

Spectral Imaging System Performance Forecasting

John P. Kerekes
Sensor Technology and System Applications Group
MIT Lincoln Laboratory
244 Wood St., Lexington, MA 02420
(781) 981-0805, kerekes@ll.mit.edu

Abstract - The quantitative forecasting of spectral imaging system performance is an important capability at every stage of system development including system requirement definition, system design, and even sensor operation. However, due to the complexity of the end-to-end remote sensing system involved, the analyses are often performed piecemeal by various groups, and then merged together. The ability to understand system sensitivities also supports the best use of an operational system and is thus desirable.

It was with this perspective and goal to better perform end-to-end remote sensing system analyses that work was undertaken in the late 1980's to develop models that can be efficiently used as part of the system design and operation. Both simulation and analytical models were developed. The simulation approach has the advantage of creating an actual image, which can include non-linear effects or specified instrument artifacts, while the analytical approach has the benefit of being much simpler computationally and amenable to large numbers of comprehensive trade studies.

In the mid 1990's, the analytical approach was extended to the case of unresolved object detection. By taking advantage of the spectral information, objects and materials that are not spatially resolved in the imagery can still be detected and identified. Subsequently, this model, which was developed for the reflective solar part of the optical spectrum, was extended to the thermal infrared. Here, surfaces are characterized not only by their spectral emissivity means and covariances, but also their physical temperature mean and standard deviation. The model has also been extended to explore linear unmixing applications through the implementation of multiple classes in the target class. This has allowed the exploration of the role of class variability in unmixing abundance estimation.

This paper provides an overview of this model development activity as well as show examples of how it can be used in the various applications. Examples include the impact of system parameters sub-pixel object detection and abundance estimation applications. Key capabilities as well as limitations of this analytical modeling approach are identified. System understanding developed through the use of the model is highlighted and the future enhancements are discussed.

I. INTRODUCTION

The quantitative forecasting of spectral imaging system performance is an important capability at every stage of system development including system requirement definition, system design, and even sensor operation. The ability to accurately predict the effects on utility of the data due to scene conditions, sensor performance, or even algorithm parameters is desirable. However, due to the complexity of

the end-to-end remote sensing system involved, the analyses are often performed piecemeal by various groups, and then merged together. Scene characteristics are often defined by science investigators, and handed off to engineers who design the instrument. The data analysis algorithm developers are then left to design their algorithm to work with the resulting data characteristics, often with little opportunity for interaction amongst the system components. While this approach is sometimes unavoidable due to programmatic constraints, it is clearly undesirable from the perspective of obtaining an "optimum" design. The ability to understand system sensitivities also supports the best use of an operational system and is thus desirable.

It was with this perspective and goal to better perform end-to-end remote sensing system analyses that work was undertaken in the late 1980's to develop models that can be efficiently used as part of the system design and operation. Both simulation [1] and analytical [2] models were developed. The simulation approach has the advantage of creating an actual image, which can include non-linear effects or specified instrument artifacts, while the analytical approach has the benefit of being much simpler computationally and amenable to large numbers of comprehensive trade studies. The analytical approach was applied at that time to the study of parameter sensitivity for a proposed hyperspectral imaging system. This earlier work evaluated the quantitative sensitivity of landcover classification accuracy to such system parameters as calibration error, solar zenith angle, as well as feature selection [3].

In the mid 1990's, the analytical approach was extended to the case of unresolved object detection [4]. This application of hyperspectral imaging systems has emerged as a unique capability by which extended mapping of an area can be accomplished through relaxation of spatial resolution requirements leading to larger swaths and area coverage rates. By taking advantage of the spectral information, objects and materials that are not spatially resolved in the imagery can still be detected and identified. In the analytical approach the various classes of interest in the scene are characterized by their spectral reflectance mean vectors and covariance matrices. The sub-pixel objects are placed in a background class through the use of a linear mixing model. The end-to-end model has been exercised to study the interrelationships between system parameters in this application. Quantitative sensitivities have been developed to

¹This work was sponsored by the Department of Defense under Contract F19628-00-C-0002. Opinions, interpretations, conclusions, and recommendations are those of the authors and are not necessarily endorsed by the United States Government.

major system parameters including ground resolution, sensor signal-to-noise ratio, and number of spectral channels.

Subsequently, this model, which was developed for the reflective solar part of the optical spectrum, was extended to the thermal infrared [5]. Here, surfaces are characterized not only by their spectral emissivity means and covariances, but also their physical temperature mean and standard deviation. The model has also been extended to explore linear unmixing applications through the implementation of multiple classes in the target class [6]. This has allowed the exploration of the role of class variability in unmixing abundance estimation.

This paper provides an overview of this model development activity as well as show examples of how it can be used in the various applications. Examples include the impact of system parameters on sub-pixel object detection and abundance estimation applications. Key capabilities as well as limitations of this analytical modeling approach are identified. System understanding developed through use of the model is highlighted, and future enhancements are discussed.

II. END-TO-END SYSTEM MODEL

The end-to-end remote sensing system model includes the scene (illumination, surface, and atmospheric effects), the sensor (spatial, spectral, and radiometric effects), and the processing algorithms (calibration, feature selection, application algorithm) that produce a data product. Fig. 1 presents an overview of the model.

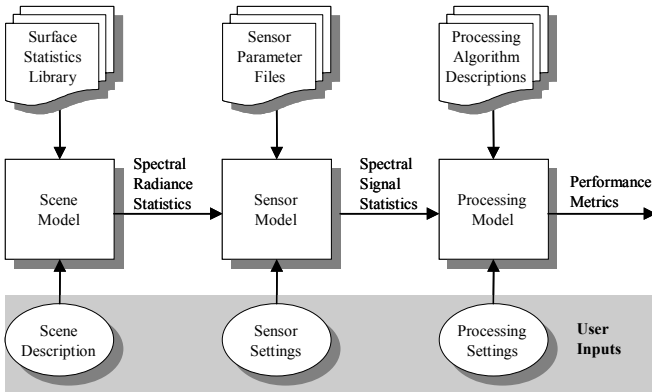


Figure 1. Block diagram of the end-to-end remote sensing system model.

The underlying premise of the model is that the various surface classes of interest can be represented by first- and second-order spectral and temperature statistics and that the effects of various processes in the end-to-end spectral imaging system can be modeled as transformations and functions of those statistics.

The model is driven by an input set of system parameter descriptions that define the scenario, including the scene classes, atmospheric state, sensor characteristics, and processing algorithms.

These parameters are used in analytical functions to transform the spectral reflectance and surface temperature first- and second-order statistics of each class through the spectral imaging process. The spectral mean and spectral covariance matrix of each class is propagated from the surface to spectral radiance to sensor signals and, then, to features, where they are operated on to achieve a metric of system performance. The following section describes the scene, sensor, and processing components of the model.

III. MODEL COMPONENTS

A. Scene Model

The model considers a scene to consist of one, or more, background classes and a spatially unresolved target object class. The user supplies the proportion of the scene filled by each background class and the fraction of a pixel occupied by the object class. Each class is described by its first- and second-order spectral reflectance statistics (mean and covariance) in the reflective solar region (0.4 to 2.5 μm), and by its spectral emissivity and temperature statistics in the thermal infrared (3 to 14 μm). Currently, we do not consider the case of simultaneous solar illumination and thermal radiation. Weighted combinations of these spectral vectors and matrices, along with descriptions of the atmosphere and the observation geometry, are transformed by an atmospheric code into surface-reflected and path-scattered radiances. These radiances are then combined to produce the mean and covariance statistics of the spectral radiance at the input aperture of a spectral imaging sensor.

Notional scene geometry and sub-pixel object model. The model assumes a simple area-weighted linear mixing model for a sub-pixel object within a scene that contains one or more background classes, as shown in Fig. 2. Each of the M background classes occupies a fraction f_m of the scene, with the constraint the fractions sum to one. The sub-pixel object is considered to be embedded within one of these classes, denoted m^* . It is important to note that this model does not actually simulate a specific spatial layout, but rather accounts for the effects of the multiple background classes through the area-weighting scheme.

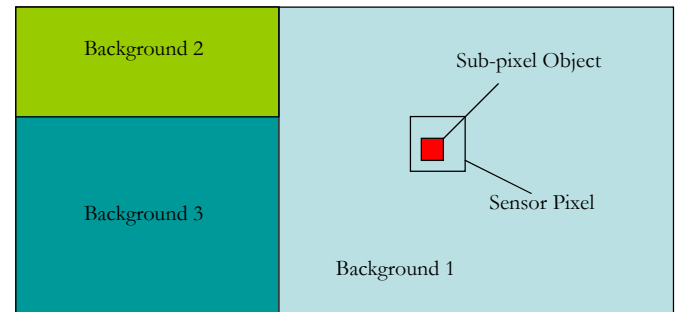


Figure 2. Notional scene geometry with multiple background classes and a subpixel object.

A simple linear mixing model is assumed for the object-class pixel. The sub-pixel fraction f_T ($0 < f_T \leq 1$) defines the

fractional area of the pixel occupied by the object with direct line-of-sight to the sensor. Parts of the object occluded by the background are accounted for in the background fraction.

The model has been generalized to allow for the target object pixel to be composed of multiple classes. The model for the P class target pixel uses the scalar class abundances a_p , $0 \leq a_p \leq 1$, $\sum a_p = 1$, $p=1 \dots P$, to weight the mean reflectance vectors ρ_p (or emissivity in the thermal infrared) and covariances matrices Σ_{pp} as shown in (1) and (2) for the multiple class target.

$$\rho_T = \sum_{p=1}^P a_p \rho_p \quad (1)$$

$$\Sigma_{\rho T} = \sum_{p=1}^P a_p^2 \Sigma_{pp} \quad (2)$$

The transformation from surface statistics to at-sensor spectral radiance statistics is performed using different equations depending on whether the system being modeled is in the solar reflective spectral region or the thermal emissive infrared. In both cases, the Air Force Research Laboratory radiative transfer code MODTRAN [7] is used to calculate the atmospheric transmittance and radiance functions.

Solar Illumination Only. The reflectance statistics are then converted to at-sensor spectral radiance L statistics for the target pixel as in (3) and (4). Note, the scalar fraction f_T is used to model the P -class target object as sub-pixel in background B . The subscript S refers to surface reflected radiance, while the subscript P refers to atmospheric path scattered radiance. The subscripts I and 0 are used to denote the surface albedo used in the radiance calculations. The radiance statistics for the background classes are transformed similarly for each class individually.

$$L_T = L_S [f_T \rho_T + (1 - f_T) \rho_B] + L_P [\rho_{Bave}] \quad (3)$$

$$\begin{aligned} \Sigma_{LT} = & f_T^2 \Lambda_{LSI} \Sigma_{\rho T} \Lambda_{LSI} + \\ & (1 - f_T)^2 \Lambda_{LSI} \Sigma_{\rho B} \Lambda_{LSI} + \\ & (\Lambda_{LP1} - \Lambda_{LP0}) \Sigma_{\rho Bave} (\Lambda_{LP1} - \Lambda_{LP0}) \end{aligned} \quad (4)$$

Thermal Infrared Emission Only. The scene thermal radiance model considers a scene to consist of one or more background classes and one target class. Currently, the target object is considered to be subpixel or at most occupy a single pixel and is restricted to consist of only one class. As in the reflective solar only case, each class is defined by the fraction of the scene occupied by that class and a set of statistics. The input statistics for each class include the mean temperature \bar{T} , the temperature variance σ_T^2 , the mean spectral emissivity $\bar{\epsilon}_\lambda$, and the full spectral emissivity covariance matrix Σ_ϵ . The following equations describe how these

surface statistics are transformed into at-sensor radiance statistics.

The at-sensor spectral radiance has three terms in the LWIR as shown in (5). The first represents the surface emitted radiance, the second is the reflected downwelling radiance, and the third is the atmospheric emitted upwelling radiance.

$$L_{\lambda, Sensor} = \tau_\lambda \epsilon_\lambda B_\lambda(T) + \tau_\lambda (1 - \epsilon_\lambda) L_{\lambda, Down} + L_{\lambda, Up} \quad (5)$$

Where,

- τ_λ = atmospheric transmittance from the surface to the sensor,
- ϵ_λ = surface spectral emissivity,
- $B_\lambda(T)$ = Planck radiance function for temperature T ,
- $L_{\lambda, Down}$ = atmospheric emitted downwelling radiance, and
- $L_{\lambda, Up}$ = atmospheric emitted upwelling radiance.

The various components are computed using MODTRAN, or simply through the Planck radiance equation. The spectral radiances for the target and background are computed using separate MODTRAN runs with the appropriate mean surface emissivity and mean temperature. For subpixel targets with subpixel fraction f , these components are linearly combined as in (6).

$$L_{\lambda, Sensor, Total} = f L_{\lambda, Sensor, Target} + (1 - f) L_{\lambda, Sensor, Background} \quad (6)$$

The at-sensor spectral radiance covariance matrix was derived by computing the expectation of the scene radiance defined in equation (5) with the mean subtracted times the transpose of that quantity as shown in (7).

$$\Sigma_{\lambda, Sensor} = E \{ [L_{\lambda, Sensor} - \bar{L}_{\lambda, Sensor}] [L_{\lambda, Sensor} - \bar{L}_{\lambda, Sensor}]^T \} \quad (7)$$

In the derivation, an assumption was made that the surface temperature of the object is uncorrelated with its spectral emissivity. This is not strictly true, as thermal cooling is dependent upon emissivity (among other parameters) and emissivity is often related to the solar albedo, which can govern the object's temperature during the day. However, these assumptions make the computations tractable and are not seen as overly restrictive to adequately characterize the variability in the spectral radiance. The resultant expression has six terms as shown in (8) for whole pixel objects. All terms are $N \times N$ where N is spectral dimensionality of the data.

$$\Sigma_{Sensor} = \mathbb{T} [\Lambda_{\sigma_L} \Sigma_{\epsilon_s} \Lambda_{\sigma_L} + \Lambda_{\bar{L}_s} \Sigma_{\epsilon_s} \Lambda_{\bar{L}_s} + \Lambda_{\bar{\epsilon}_s} \Sigma_{L_s} \Lambda_{\bar{\epsilon}_s} +$$

$$\Lambda_{L_D} \Sigma_{\epsilon_s} \Lambda_{L_D} - (\Lambda_{L_D} \Sigma_{\epsilon_s} \Lambda_{\bar{L}_s} + \Lambda_{\bar{L}_s} \Sigma_{\epsilon_s} \Lambda_{L_D})] T \quad (8)$$

Where,

- T = diagonal matrix of surface-to-sensor atmospheric transmittance,
- Λ_{σ_L} = diagonal matrix of surface emitted spectral radiance standard deviation with each entry $\sigma_L = \sigma_T \partial B / \partial T$ for $T = \bar{T}$, where σ_T is the surface temperature standard deviation and $\partial B / \partial T$ is the derivative of the Planck radiance function,
- Σ_{ϵ_s} = full spectral emissivity covariance matrix,
- $\Lambda_{\bar{L}_s}$ = diagonal matrix of mean Planck radiance emitted by the surface (assumes black body surface),
- Σ_{L_s} = spectral covariance of surface emitted radiance (= $\Lambda_{\sigma_L} [1] \Lambda_{\sigma_L}$, where [1] is a $N \times N$ matrix of ones),
- $\Lambda_{\bar{\epsilon}_s}$ = diagonal matrix of mean surface emissivity,
- Λ_{L_D} = diagonal matrix of downwelling radiance.

For subpixel thermal targets, the whole pixel covariances are weighted by a function of the target subpixel fraction f_T as in (9).

$$\Sigma_{Sensor, Total} = f_T^2 \Sigma_{Sensor, Target} + (1 - f_T)^2 \Sigma_{Sensor, Background} \quad (9)$$

B. Sensor Model

The sensor model takes the spectral radiance mean and covariance statistics for the various ground classes and applies sensor effects to produce signal mean and covariance statistics that describe the scene as imaged by an imaging spectrometer. The sensor model includes a limited number of radiometric noise sources, with no spatial or spectral sources of error included. Also, as was noted earlier, the channel spectral response of the sensor is applied during the input radiance calculations described in the previous section.

Radiometric noise processes are modeled by adding variance to the diagonal entries of the spectral covariance matrices. Off-diagonal entries are not modified, based on the assumption that there is no channel-to-channel correlation in the noise processes.

The radiometric noise sources come from detector noise processes, including photon (shot) noise, thermal noise, and multiplexer/readout noise. Since detector parameters are often specified in terms of electrons, the noise terms are summed in a root sum squared sense in that domain before being converted to noise equivalent spectral radiance.

The total detector noise is then calculated as the root-sum-square of the photon noise σ_{np} , the thermal noise σ_{nt} , and the multiplexer/readout noise σ_{nm} .

The total detector noise σ_n (in electrons) is then converted back to noise equivalent spectral radiance σ_{Ln} and scaled by a user-specified noise factor g_n before being added to the diagonal entries of the spectral covariance matrices for each sensor spectral channel.

Another noise source is relative calibration error c_R . This error is also assumed to be uncorrelated between spectral channels, with a standard deviation σ_{CR} expressed as a percentage of the mean signal level. This error, expressed as a variance, σ_{CR}^2 , is added to the diagonal entries of the covariance matrices of each class, as with the other noise sources.

The last two noise sources are the quantization noise in the analog-to-digital conversion and bit errors in the communications or data recording system. These both depend upon the assumed dynamic range of the sensor L_{max} . The quantization error variance is calculated as shown in (10) for a system with Q radiometric bits.

$$\sigma_{nq}^2 = \frac{1}{12} \left(\frac{L_{max}}{2^Q - 1} \right)^2 \quad (10)$$

The model for the effect of bit errors in the data link (or on-board storage) assumes that bit errors are uniformly distributed across the data word and could be of either sign. Thus, for Q bits, the error will take on one of $2Q$ values, $\pm 2^i$ for $i=0, \dots, Q-1$, with equal probability of $1/(2Q)$. The noise variance, σ_{nBe}^2 , due to a bit error rate of B_e is shown in (11).

$$\sigma_{nBe}^2 = \frac{B_e}{Q} \sum_{q=0}^{Q-1} \left(2^q \frac{L_{max}}{2^Q - 1} \right)^2 \quad (11)$$

These last two noise terms σ_{nq}^2 and σ_{nBe}^2 are also added to the diagonal entries of the spectral covariance matrices.

For reporting as a performance metric, the class-dependent sensor signal-to-noise ratio (SNR) is calculated as the ratio between the mean signal and the square root of the sum of the noise variance terms.

C. Processing Model

The processing model takes the sensor output class statistics and computes a performance metric. There are three steps in this process: atmospheric compensation (optional and only implemented for the reflective solar spectral region), feature extraction, and performance metric computation.

Atmospheric Compensation. Atmospheric compensation is accomplished by using low and high reflectance surrogate calibration panels and computing the slope m and offset o with a two-point linear fit between the mean panel signal and the known reflectance. This models the widely used empirical line method (ELM) for atmospheric compensation.

The slopes and offsets are applied to the mean signal and covariance matrices of the various target and background

classes to compute the retrieved (or estimated) class reflectance mean $\hat{\rho}$ and covariance $\hat{\Sigma}$ statistics. The spectral characterization accuracy is described by the mean difference, SC_{bias} , between the retrieved surface reflectance of the target and the initial known reflectance, and by the standard deviation, σ_{SC} , of the difference for each spectral channel l , as in (12) and (13).

$$SC_{bias}(l) = \hat{\rho}(l) - \rho(l) \quad (12)$$

$$\sigma_{SC}(l) = \sqrt{\hat{\sigma}_\rho^2(l, l) - \sigma_\rho^2(l, l)} \quad (13)$$

Feature Selection. Several options are available for extracting a reduced dimensionality feature vector from the signal vector. These include: 1) all channels within contiguous region(s), (e.g., to avoid water vapor absorption spectral regions), 2) principle components, or 3) band averaging to simulate multispectral channels. All options are implemented as a linear transformation using a feature selection matrix Ψ . This matrix is applied to both the mean vectors and the covariance matrices in the retrieved reflectance domain (if atmospheric compensation was performed) or in the signal domain directly on the statistics output by the sensor model.

$$F_i = \Psi^T X_i \quad (14)$$

$$\Sigma_{F_i} = \Psi^T \Sigma_{X_i} \Psi \quad (15)$$

In (14) and (15), the variable X refers to the signal type (retrieved reflectance or sensor signal) and the index i refers to the various target and background classes.

Performance Metrics. Three algorithms are available to determine a performance metric for a given scenario: 1) a version of the spectral matched filter known as Constrained Energy Minimization (CEM) [8], 2) Total Error [9], and 3) linear unmixing [10]. CEM can be used to predict P_D/P_{FA} curves. Total Error approximates classification error or the sum of false alarm and missed detection probabilities and is used as a metric to measure relative impacts on performance during parameter trade studies. Linear unmixing allows assessment of the variability in abundance estimates due to class variability.

The CEM operator uses a known target ‘‘signature’’ and an estimate of the background spectral covariance to minimize the energy from the background and to emphasize the desired target. In the model, the known ‘‘signature’’ is actually the unmodified original target mean reflectance used at the input to the model. The operator w is formed as shown in equation (16), where the subscript F indicates the signal means and covariances have been transformed to the desired feature space using equations (14) and (15).

$$w = \frac{\hat{\Sigma}_{\rho FBave}^{-1} (\rho_{FT} - \hat{\rho}_{FBave})}{(\rho_{FT} - \hat{\rho}_{FBave})^T \hat{\Sigma}_{\rho FBave}^{-1} (\rho_{FT} - \hat{\rho}_{FBave})} \quad (16)$$

This operator w is used to transform the means and covariances from the feature space to a scalar test statistic with mean θ and variance σ_θ^2 , from which the P_D/P_{FA} curve can be calculated. The operator is applied to the combined target/background features and to the features of each of the background classes as shown in the following set of equations.

$$\theta_T = w^T (\hat{\rho}_{FT} - \hat{\rho}_{FBave}) \quad (17)$$

$$\theta_{Bm} = w^T (\hat{\rho}_{FBm} - \hat{\rho}_{FBave}) \quad \text{for } m = 1 \dots M \quad (18)$$

$$\sigma_{\theta_T}^2 = w^T \hat{\Sigma}_{\rho FT} w \quad (19)$$

$$\sigma_{\theta_{Bm}}^2 = w^T \hat{\Sigma}_{\rho FBm} w \quad \text{for } m = 1 \dots M \quad (20)$$

The probability of detection P_{Dm} (computed separately for each background class m) is then computed for a specified probability of false alarm P_{FA} , using a Gaussian assumption for the test statistic output by the CEM operator. This assumption is loosely justified by the Central Limit Theorem since the operator is really just the summation of a large number of random variables. The threshold h_m is determined from the desired probability of false alarm and mean θ_{Bm} and variance $\sigma_{\theta_{Bm}}^2$ for each background class m . The function Φ^{-1} returns the cutoff value such that the area under the standard normal curve to the right of the cutoff is equal to the argument of the function.

$$h_m = \theta_{Bm} + \sigma_{\theta_{Bm}} \Phi^{-1}(P_{FA}) \quad (21)$$

$$P_{Dm} = \frac{1}{\sigma_{\theta_T} \sqrt{2\pi}} \int_{h_m}^{\infty} \exp\left[-\frac{(x - \theta_T)^2}{2\sigma_{\theta_T}^2}\right] dx \quad (22)$$

For scenarios with multiple backgrounds, the threshold h^* yielding the minimum P_D is used to recompute the P_{FA} 's for the other classes. These new P_{FA} 's are then summed using the background class area fractions f_m to yield a combined P_{FA} . The combined P_D is simply the minimum P_{Dm} .

$$P_{FA} = \sum_{m=1}^M f_m P_{FAm}(h^*) \quad (23)$$

$$P_D = \min P_{Dm} \quad (24)$$

The total error metric approximates the total error P_e (i.e., the overlap between multivariate distributions) in a two-class equal *a priori* probability case as shown in (25).

$$P_e \approx \frac{1}{2}(1 - P_D) + \frac{1}{2}P_{FA} \quad (25)$$

While P_e does not distinguish between errors due to false alarms or missed detections, it does provide a single scalar metric that can be used for relative performance comparisons. It is normally used to calculate the relative contribution to system error from the various system parameters. P_e is

calculated using the standard normal error function and the Bhattacharyya distance B ,

$$P_e = \frac{1}{\sqrt{2\pi}} \int_{\frac{x^2}{2}}^{\infty} \exp\left(-\frac{x^2}{2}\right) dx \quad (26)$$

where,

$$B = \frac{1}{8} (F_T - F_B)^T \left(\frac{\Sigma_{FT} + \Sigma_{FB}}{2} \right)^{-1} (F_T - F_B) + \frac{1}{2} \ln \frac{|\Sigma_{FT} + \Sigma_{FB}|}{\sqrt{|\Sigma_{FT}| |\Sigma_{FB}|}}. \quad (27)$$

For performance prediction in linear unmixing applications, we have implemented the Unconstrained Least Squares linear unmixing [10] algorithm. This metric is only available for analyses run in the reflective solar spectral region. Estimates of the mean fractional abundances \hat{A} of the endmembers in the target pixel are calculated as shown in (28) where \mathbf{S} is the matrix of the original endmembers (selected bands) as shown in (29).

$$\hat{A} = (\mathbf{S}^T \mathbf{S})^{-1} \mathbf{S}^T \hat{\rho}_T \quad (28)$$

$$\mathbf{S} = [\rho_1 \rho_2 \dots \rho_P] \quad (29)$$

The variances of the abundance estimates are calculated using the same unmixing operator, but applied to the estimated covariance. The variances are the diagonal elements of $\hat{\Sigma}_A$ calculated as shown in (30).

$$\hat{\Sigma}_A = [(\mathbf{S}^T \mathbf{S})^{-1} \mathbf{S}^T] \hat{\Sigma}_{\rho T} [(\mathbf{S}^T \mathbf{S})^{-1} \mathbf{S}^T]^T \quad (30)$$

IV. VALIDATION

The model and its implementation have been validated with airborne hyperspectral imagery. A recent publication [4] included comparisons of measured data and model predictions at several points in the end-to-end spectral imaging process. These included the spectral radiance at the sensor input aperture, the sensor signal-to-noise ratio, and the detection performance (P_D/P_{FA}) after application of a spectral matched filter. At all points in the process the model predictions compare closely to the empirical data.

V. EXAMPLE ANALYSIS RESULTS

To illustrate use of this model, we present three example analyses showing performance predictions and parameter sensitivities. The first example shows the sensitivity to atmospheric and sensor parameters of unresolved road detection. The second predicts accuracy and variability in abundance estimates and their sensitivity to various system parameters. The third example shows detection sensitivities for a calibration panel with a thermal infrared spectral sensor.

Example 1: Sub-pixel road detection sensitivity to system parameters. One use of the model is to study how sensitive a given sensor might be to either design changes or scene conditions. This type of analysis can be helpful when setting system requirements or when setting data collection parameters for systems which have controllable parameters.

To illustrate this use of the model, we present results of two analyses showing parameter sensitivities. The scenario for both is the detection of a sub-pixel road in a forested background, with the use of a road spectrum (from a library or previous data collection) and a spectral matched filter. The analysis uses a model for the Hyperion [11] sensor, and an atmospheric compensation algorithm with 1% (1 σ) accuracy.

In the examples given below, the results are presented as the probability of detection (at a constant false alarm rate) as a function of the fraction of a pixel occupied by the road. This pixel fill fraction can be loosely translated to an actual object size, given a pixel ground resolution, assuming the object is not split across adjacent pixels. As an example, Fig. 3 presents a graphic showing how a 15 meter wide road running through the middle of a 30 meter resolution pixel would roughly correspond to a 50% fill factor, ignoring the detailed effects of sensor and atmospheric point spread functions. Because the model assumes a linear mixing of the object and the background class, we can present P_D as a function of this pixel fill fraction and avoid specifying a particular sensor spatial resolution and object size. Thus, the analysis results can be applied to a range of absolute ground resolutions and object sizes, although the exact performance will vary because of sensor noise considerations and the variability of the spectral statistics at the various resolutions.

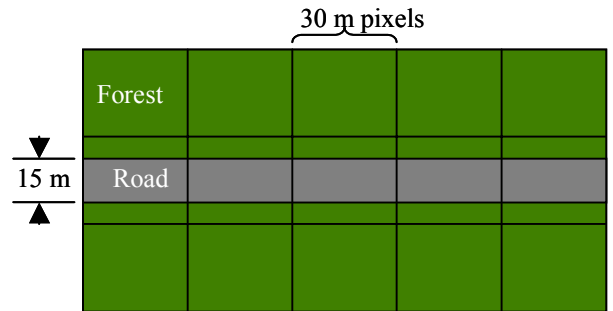


Figure 3. Overhead view showing 50% fill factor for road in forest example.

Changes in atmospheric visibility, specified by the meteorological range parameter, will affect the signal level in a spectrally-dependent manner, as well as affect the amount of radiance scattered from the background into the object pixel. Even though the scenario includes an atmospheric compensation step, this scattered radiance can affect performance. Fig. 4 shows that the required fill fraction f_T for a high detection probability ($P_D \geq 0.9$) increases with decreasing meteorological range. However, the increase in required f_T is relatively moderate (30% to 40%) for a significant decrease (80 km to 5 km) in the meteorological

range. Thus, in this scenario, one can conclude that detection performance is only moderately affected by atmospheric haze over a reasonable range of values.

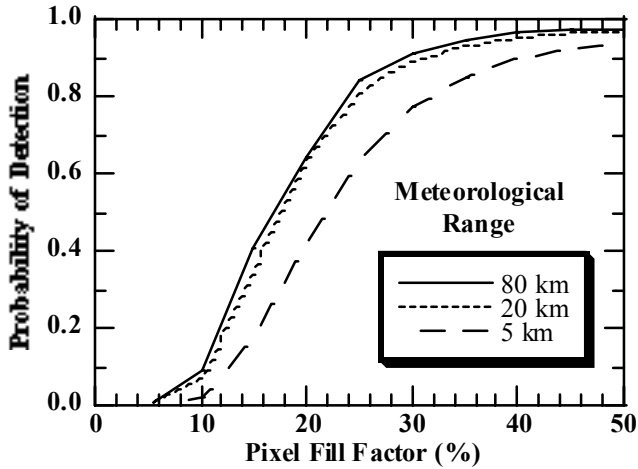


Figure 4. Sensitivity of road detection to atmospheric meteorological range as a function of pixel fill factor.

The effects of random error in the next analysis is studied by adding zero-mean “noise” with a standard deviation equal to a user-specified percentage of the mean radiance. In a real sensor system, this random error could come from a number of sources such as residual non-uniformity correction error or random errors in the atmospheric compensation¹. Fig. 5 presents the sensitivity of detection probability to random errors of 0%, 1%, 2%, or 4% of the mean signal level. This range of additive error is typical for state-of-the-art sensors, non-uniformity correction routines, and atmospheric compensation algorithms. As in the previous example, for this range of values, the detection performance sensitivity is moderate, with the required ($P_D \geq 0.9$) fill fraction changing from 30% to 40%, as 4% additional error is added.

Example 2: Linear unmixing abundance variability estimation. The end-to-end modeling approach allows one to easily change system parameters and study the resulting effect on product accuracy. Numerous sources can contribute to errors in unmixing abundance estimates, including scene complexity, number and abundance of endmembers, material variability, non-linear mixing, atmospheric effects, sensor radiometric noise and calibration error, spatial point spread function effects, spectral calibration errors, endmember misidentification and spectral channel selection.

¹ Another way to interpret these error levels is to recognize that with the additive error, the spectral radiance in each spectral channel has a signal-to-noise ratio hard limited to the inverse of the additive error. For example, with 2% random error added, the SNR cannot be higher than 50.

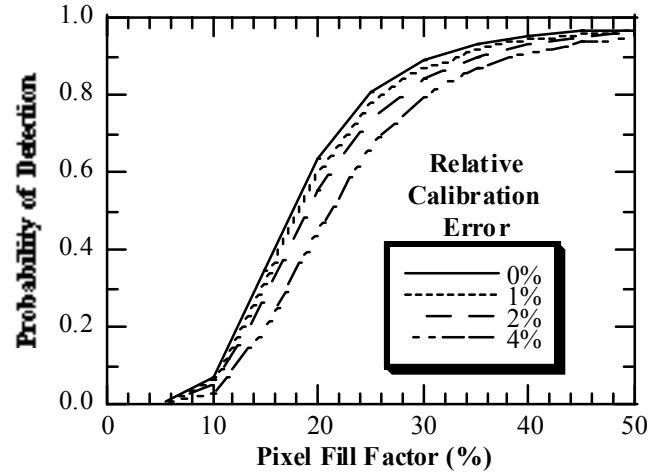


Figure 5. Sensitivity of road detection to additional (beyond sensor detector and electronics noise) random error (with a standard deviation expressed as a percentage of the mean signal) as a function of pixel fill factor.

Several studies were conducted with the model to explore the impact of a number of these potential error sources. In these examples, we have a two-class mixing problem: building roof and parking lot. Hyperion is the assumed sensor as in the previous example. In Table I we see that by setting the input covariances of the class statistics to zero, the standard deviation of the retrieved abundance estimates approach zero. Table II shows that by leaving the covariance alone and setting the instrument noise to zero, there is negligible effect on the standard deviation. These results demonstrate that for the typical values in this scenario, the natural variability (material reflectance covariance) has more impact on the spread of the abundance estimates than does sensor noise.

TABLE I
MODEL PREDICTED ABUNDANCE WITH INPUT CLASS REFLECTANCE COVARIANCE SET TO ZERO COMPARED TO DEFAULT CASE

Material Class	Default Covariance Mean $\pm 1\sigma$	Covariance = 0 Mean $\pm 1\sigma$
Building roof	0.49 \pm 0.04	0.49 \pm 0.00
Parking lot	0.53 \pm 0.17	0.53 \pm 0.01

TABLE II
MODEL PREDICTED ABUNDANCE WITH SENSOR NOISE SET TO ZERO COMPARED TO DEFAULT CASE

Material Class	Default Noise Mean $\pm 1\sigma$	Sensor noise = 0 Mean $\pm 1\sigma$
Building roof	0.49 \pm 0.04	0.49 \pm 0.04
Parking lot	0.53 \pm 0.17	0.53 \pm 0.17

Table III shows an expected decrease in predicted mean abundance with a -5% absolute radiometric calibration error. Table IV shows the significant impact on the abundance estimates of using only 43 VNIR channels compared to the 117 selected from the full VNIR and SWIR spectrum.

TABLE III
MODEL PREDICTED ABUNDANCE WITH -5% ABSOLUTE RADIOMETRIC CALIBRATION ERROR IN SENSOR COMPARED TO DEFAULT CASE

Material Class	Zero Error Mean $\pm 1\sigma$	-5% Calibration Error Mean $\pm 1\sigma$
Building roof	0.49 \pm 0.04	0.46 \pm 0.04
Parking lot	0.53 \pm 0.17	0.50 \pm 0.16

TABLE IV
MODEL PREDICTED ABUNDANCE USING ONLY 43 VNIR SPECTRAL CHANNELS COMPARED TO DEFAULT CASE

Material Class	136 VNIR/SWIR Mean $\pm 1\sigma$	43 VNIR Only Mean $\pm 1\sigma$
Building roof	0.49 \pm 0.04	0.44 \pm 0.23
Parking lot	0.53 \pm 0.17	0.68 \pm 0.76

The last experiment in the unmixing analysis was to include several endmembers in the abundance inversion that were not present in the modeled pixel of interest. Table V shows the result for the unconstrained unmixing algorithm for this case. We note the retrieved abundance for the parking lot is significantly different not only in the mean, but also in its standard deviation. This provides an example of the kind of errors that can be observed when improper assumptions of endmembers are used in the unmixing analysis.

TABLE V
MODEL PREDICTED ABUNDANCE USING ADDITIONAL ENDMEMBERS IN THE UNMIXING OPERATOR WHICH WERE NOT PRESENT IN THE TEST PIXEL COMPARED TO DEFAULT CASE

Material Class	Two Endmembers Mean $\pm 1\sigma$	Seven Endmembers Mean $\pm 1\sigma$
Building roof	0.49 \pm 0.04	0.49 \pm 0.11
Parking lot	0.53 \pm 0.17	0.63 \pm 1.49
Healthy vegetation	N/A	-0.09 \pm 0.36
Gravel road	N/A	0.06 \pm 0.14
Paved road	N/A	-0.22 \pm 1.73
Bare hillside	N/A	-0.05 \pm 0.08
Green grass	N/A	0.07 \pm 0.20

Example 3: Objection detection sensitivities in the thermal infrared. This example models a large calibration panel on a grass background being observed by the SEBASS LWIR sensor [12] in a scenario of detecting the panel using a pre-computed radiance signature and the CEM matched filter. In this example, the calibration panel was initially set at a slightly higher temperature than the grass background (23.75°C vs. 22.0°C). However, the panel had a lower emissivity (0.95-0.98 spectrally varying vs. 0.99 spectrally constant). To study the effect of target/background mean temperature differences on detection performance, the background mean temperature was held constant while the target temperature was raised and detection performance computed. Fig. 6 presents the results that show a clear minimum at a temperature difference (target-background) of 1.4°C. At this value, the combination of a higher target temperature and a lower emissivity result in nearly equal mean spectral radiances for the target and background, leading to a minimum in detection performance. Temperature differences higher or lower lead to more contrast, and thus greater detection probabilities.

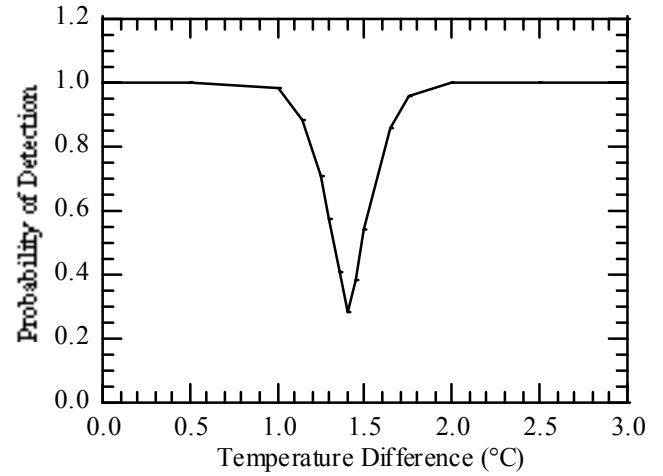


Figure 6. Detection performance sensitivity to target/background mean temperature difference.

To study the effect of target temperature variability, the temperature standard deviation of the calibration panel was varied from 0.0 to 1.0 °C while all other parameters were held constant. Fig. 7 presents the results, which show the decrease in detection performance as the target temperature variability increases.

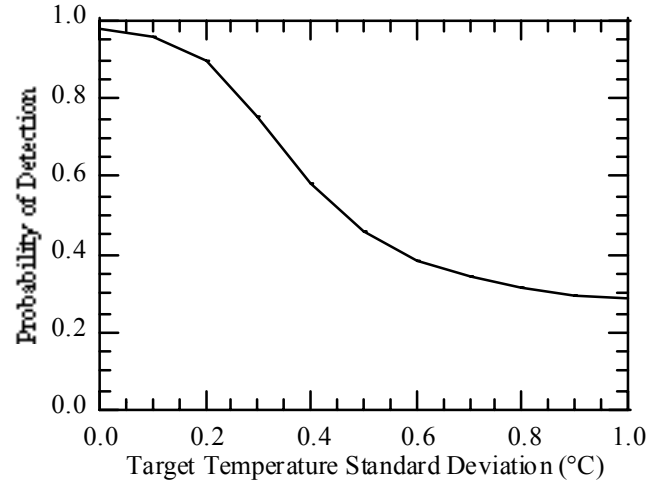


Figure 7. Detection performance sensitivity to target temperature variability.

VI. SUMMARY AND CONCLUSIONS

An approach has been presented to predict detection performance and analyze system parameter sensitivities for multispectral or hyperspectral sensors. The end-to-end system model builds on a previously developed approach using first- and second-order spectral statistics and transformations of those statistics to predict performance. The model includes a linear mixing model for the sub-pixel objects, reflected solar or thermal emission surface and atmospheric models, radiometric sensor modeling capability, atmospheric

compensation approaches, a matched filter detection algorithm, and a linear unmixing algorithm. Unlike image simulation models, this model does not produce a simulated image, but rather predicts detection or error probabilities, and the endmember abundance variability in unmixing applications. Thus, our model avoids the computational requirements for pixel-by-pixel ray tracing of simulation approaches.

The model has been, and continues to be, validated by showing good agreement between predictions and measurements of spectral radiances, sensor SNR's, and detection probabilities derived from airborne hyperspectral sensor data.

Several example analyses were presented to show how the model has been used to predict performance and explore parameter sensitivities. Examples were presented predicting unresolved road detection performance sensitivity to atmospheric and sensor parameters. Sensitivity to parameters in an unmixing application was also explored. Also, detection sensitivities in a thermal infrared observation scenario were examined. In these examples, the most important and most sensitive parameters were characteristics of the surface classes and environmental conditions of the scene, rather than sensor parameters or algorithmic choices. Certainly, though, situations exist where these parameters or choices can have significant effect.

The model has many advantages over other performance prediction tools, including quick execution, which enables extensive trade studies to be conducted expeditiously. It does, however, have a number of limitations, some of which can be addressed with further development, while others are inherent in the analytical approach. Limitations that are inherent include the inability to model specific geometries of scene objects or materials, especially those that involve multiple reflections, and sensor artifacts or processing algorithms that involve non-linear operations.

Limitations of the model that we plan to address through additional development include implementation of additional sensor types and artifacts (e.g., Fourier transform instruments, spectral jitter) and processing algorithms (e.g., physics-based atmospheric compensation, anomaly detection, linear unmixing, material identification). Also, we continue to assess the appropriate statistical distributions for various classes of hyperspectral data, as well as develop confidence intervals for detection probability predictions using appropriate models for the variability of the contributing factors.

Even as the model continues to be developed, it has been useful in understanding the potential performance and limiting factors in spectral imaging scenarios supported by its current status. Thus, it represents a step along the path toward the ultimate goal of a comprehensive understanding necessary for the optimal design and use of remote sensing systems.

Support of this work from the Deputy Undersecretary of Defense for Science and Technology (DUSD S&T) and the Spectral Information Technology Applications Center is gratefully acknowledged. The author also expresses a sincere debt of gratitude and his appreciation for the outstanding example of leadership and guidance from Prof. David Landgrebe during graduate study.

REFERENCES

- [1] J.P. Kerekes and D.A. Landgrebe, "Simulation of Optical Remote Sensing Systems," *IEEE Transactions on Geoscience and Remote Sensing*, vol. GE-27, no. 6, pp. 762-771, November 1989
- [2] J.P. Kerekes and D.A. Landgrebe, "An Analytical Model of Earth-Observational Remote Sensing Systems," *IEEE Transactions on Systems, Man and Cybernetics*, vol. SMC 21, no. 1, pp. 125-133, January/February, 1991.
- [3] J.P. Kerekes and D.A. Landgrebe, "Parameter Tradeoffs for Imaging Spectroscopy Systems," *IEEE Transactions on Geoscience and Remote Sensing*, vol. GE-29, no. 1, pp. 57-65, January 1991.
- [4] J. Kerekes and J. Baum, "Spectral Imaging System Analytical Model for Sub-pixel Object Detection," *IEEE Transactions on Geoscience and Remote Sensing*, vol. 40, no. 5, pp. 1088-1101, May 2002.
- [5] J. Kerekes, M. Griffin, J. Baum, K. Farrar, "Modeling of LWIR Hyperspectral System Performance for Surface Object and Effluent Detection Applications," *Algorithms for Multispectral, Hyperspectral, and Ultraspectral Imagery VII*, SPIE vol. 4381, 2001.
- [6] J. Kerekes, K. Farrar, N. Keshava, "Linear Unmixing Performance Forecasting," *Proceedings of IGARSS'02*, Toronto, Canada, pp. 1676-1678, 24-28 June 2002.
- [7] A. Berk, L. S. Bernstein, D. C. Robertson, "MODTRAN: a moderate resolution model for LOWTRAN 7," GL-TR-89-0122, Spectral Sciences, Burlington, MA, 1989.
- [8] W. H. Farrand and J. C. Harsanyi, "Mapping the distribution of mine tailings in the Coeur d'Alene River Valley, Idaho, through the use of a constrained energy minimization technique," *Remote Sensing Environment*, vol. 59, pp. 64-76, 1997.
- [9] S. J. Whitsitt and D. A. Landgrebe, "Error estimation and separability measures in feature selection for multiclass pattern recognition," LARS Publication 082377, Laboratory for Applications of Remote Sensing, Purdue University, West Lafayette, IN, August 1977.
- [10] N. Keshava and J.F. Mustard, "Spectral Unmixing," *IEEE Signal Processing Magazine*, vol. 19, no. 1, pp. 44-57, January 2002.
- [11] J. Pearlman, et al, "Development and Operations of the EO-1 Hyperion Imaging Spectrometer," *Earth Observing Systems V*, SPIE vol. 4135, pp. 243-253, 2000.
- [12] J. Hackwell, et al, "LWIR/MWIR Imaging Hyperspectral Sensor for Airborne and Ground-Based Remote Sensing," *Imaging Spectrometry II*, SPIE vol. 2819, 1996.